Comparison between mechanisms and microstructures of α-γ, γ-ϵ, and α-ϵ-α phase transitions in iron

Robin Fréville,[1,2] Agnès Dewaele,[1,2] Nicolas Bruzy,[1,2] Volodymyr Svitlyk,[3,4] and Gaston Garbarino[3]

[1]*CEA, DAM, DIF, F-91297 Arpajon, France*

[2]*Université Paris-Saclay, CEA, Laboratoire Matière en Conditions Extrêmes, 91680 Bruyères-le-Châtel, France*

[3]*European Synchrotron Radiation Facility, BP220, 38043 Grenoble Cedex, France*

[4]*Helmholtz-Zentrum Dresden-Rossendorf, Institute of Resource Ecology, 01314 Dresden, Germany*

(Received 16 December 2022; revised 15 February 2023; accepted 1 March 2023; published 14 March 2023)

Iron $\alpha \leftrightarrow \epsilon$, $\alpha \rightarrow \gamma$, and $\gamma \rightarrow \epsilon$ transformations have been characterized in diamond anvil cells under hydrostatic compression conditions. *In situ* x-ray diffraction of single or oligocrystals and *ex situ* SEM-EBSD measurements have been analyzed with multigrain techniques. The mechanisms of $\alpha \leftrightarrow \epsilon$ transitions are martensitic, following Burgers paths which requires a high plastic activity. A memory effect of the reversion exists in the vast majority of the sample: the starting orientation of α-Fe single crystal is recovered. Small grains of α-Fe exhibit a new orientation compatible with Burgers path, possibly associated with twinning in ϵ-Fe. Close to the α-γ-ϵ-Fe triple point (8.7 GPa, 750 K), the $\alpha \rightarrow \gamma$ transformation occurs via diffusion and reconstruction of γ-Fe, and $\gamma \rightarrow \epsilon$ transformation is martensitic but involves no plasticity. As a result, the microstructures in ϵ-Fe produced by a direct $\alpha \rightarrow \epsilon$ transformation and by $\alpha \rightarrow \gamma \rightarrow \epsilon$ transitions path are very different.

DOI: 10.1103/PhysRevB.107.104105

I. INTRODUCTION

Iron is the main constituent of planetary cores and is widely used as an alloy in technological materials. Therefore its temperature- and pressure-induced phase transitions have created interest and raised many questions, especially on the involved mechanisms and the associated microstructures. Indeed, microstructures play a crucial role in determining macroscopic behavior.

At ambient conditions, Fe is stable under its α phase (body-centered cubic, bcc). Increasing the temperature initiates the formation of the γ phase (face-centered cubic, fcc) at around 1180 K. Both temperature and temperature ramp rate have a clear effect on $\alpha \leftrightarrow \gamma$ transformations mechanisms [1,2]. The reverse $\gamma \rightarrow \alpha$ phase transformation has been widely characterized by metallurgists. A rapid quench forms the martensite structure characteristic of hardened steels while slow cooling induces a diffusion-ruled transition (also called reconstructive), which indicates a switch between athermal (or martensitic) and thermally activated regimes [3,4]. The $\alpha \rightarrow \gamma$ transformation is less studied; recent work classify it as mainly reconstructive, but its exact driving forces and nature remain debated [1,5–8]. The phase transformation is observed up to $\gamma - \alpha - \epsilon$ triple point at 8.7 GPa and 750 K [9]; it becomes a ferromagnetic to paramagnetic transformation above 2 GPa, which may have an effect on its mechanism.

A pressure increase transforms α-Fe into ϵ-Fe (hexagonal close-packed, hcp) at around 13 GPa at room temperature. The transition is established as a first-order transition, with an athermal character, and associated with changes in magnetic ordering [10–13]. Information about this transition have been collected *in situ* using both dynamic compression [14–17] and static compresion, in diamond anvil cells [18–25] and Paris-Edinburgh press [8]. Evidence point to a martensitic mechanism similar to the one proposed initially by Burgers for the bcc to hcp transition in Zirconium [26]. This means a diffusionless structural transformation in a solid with clear orientation relation (OR) between the parent and daughter phases and occasionally large plastic straining observed [4]. Uncertainties about orientation relations still exist, some studies reporting that all possible orientations are observed [8,22] while others report a selection due to uniaxial straining in the case of shock compression [14–17] or static compression [25]. Sample texture role has also been highlighted [24]. The microstructure induced by the direct transition has been monitored by tomography [8], indicating an evolution from martensitic to reconstructive character as the transition proceeds. It is important to understand which features of the α-Fe $\leftrightarrow$ ϵ-Fe transition are general, and which are due to the specificities of the experiments, such as strain rate, stress tensor, sample starting microstructure, sample size and boundaries effects.

We report here *in situ* measurements with x-ray diffraction (XRD) of microstructures induced by bcc-fcc, fcc-hcp and bcc-hcp transitions in iron. The experiments have been carried out in diamond anvil cells, on single crystals or oligocrystals (a few single crystals) samples, which were hydrostatically compressed. Single crystal and multigrain analyses allow determining OR between phases. For $\alpha \leftrightarrow \epsilon$ transitions, *post mortem* microstructural observations have also been carried out. This reveals the differences between $\alpha \leftrightarrow \epsilon$, $\alpha \rightarrow \gamma$ and $\gamma \rightarrow \epsilon$ mechanisms. Comparison with literature studies suggests that although they exhibit common features, the microstructures produced by the transitions scale with sample sizes and are sensitive to strain rate.

TABLE I. PT conditions and data acquisition parameters used during our experiments. In runs 1 and 2, numbers (4) and (7) stand for the numbers of grains in polycrystalline samples. θ_{max} and θ_{step} are the maximum rotation angle of the DAC around a vertical axis, see Fig. 1(a), and its step.

Run	Beamline	θ_{max}	θ_{step}	T (K)	P (GPa)	Sample type
1	ID15b	15°	2°	300	7–13	Oligocrystal (4)
2	ID15b	20°	2°	300–809	6–17	Oligocrystal (7)
3	ID27	20°	0.25°	300–802	6–15	Single crystal
4	ID27	15°	1°	300–795	6–15	Single crystal
5	ID27	15°	1°	300–817	6–10	Single crystal
6	ID27	20°	0.5°	300–793	6–12	Single crystal
7	ID27	20°	0.5°	300–800	6–9	Single crystal
8	ID27	20°	0.5°	300–790	6–20	Single crystal

II. METHODS

A. Materials

Two types of preparations were performed. A summary is provided in Table I. Single crystals and seven-crystal sample were used to study α-γ and γ-ϵ transitions, while the four-crystal sample was used in run 1 for both direct and reverse α-ϵ transitions.

The setup used to synthesize α-Fe single crystals is similar to the one used in Ref. [9]. Single crystal samples were discs of 5–20 μm thickness to 10–60 μm diameter, with the surface normal parallel to the [001] direction, cut with pulsed laser machining [22,27] from a bulk single crystal (99.98% purity, Mateck).

For oligocrystal samples, discs of about 100-μm diameter were cut with a femtosecond laser in a laminated iron foil (99, 99+% purity, Goodfellow) of 10-μm thickness, which had been heat treated (1025 K during 8 hours under secondary vacuum followed by a slow cooling). The treatment induced the growth of α-Fe single crystals with sizes varying from 10 to 50 μm, as measured in SEM. Run 1 sample after preparation mainly consists of four crystals; run 2 sample consists of seven crystals.

All samples were loaded in a diamond-anvil cell (DAC) equipped with a 400-μm culet diamond size in order to cover the 0–35 GPa pressure range and a rhenium gasket, along with ruby for ambient temperature [28] or samarium for high-temperature experiments [29] as pressure gauge. Almax-Boehler diamond anvil cell design was used to ensure a wide angular opening. High temperatures were generated using a dedicated furnace [30]. The diamond anvil cell was placed in a resistive heating sleeve in an enclosure under primary vacuum (with kapton windows), which allows to reach 900 K on the sample. The sample temperature was measured with a K thermocouple placed in contact with the back of one diamond anvil. Neon was used as pressure transmitting medium. During high-temperature experiments, neon remained liquid ensuring hydrostatic conditions. At room temperature, it is solid above 4.8 GPa [31]. However, evidence of nonhydrostatic stresses in neon pressure medium have been collected only above 15 GPa, which remains quite close to the maximum pressure (17 GPa) reached during our room temperature experiment (run 1). This maintains a low level of nonhydrostatic stress [32].

B. X-ray diffraction

Experiments were carried out at the ID15b and ID27 beamlines of the European Synchrotron Radiation Facility (ESRF, France). Pressure and temperature were controlled with small steps (less than 1 GPa, and 10 K), especially around the expected conditions of transition. After each pressure or temperature change and after stabilization, angular dispersive x-ray diffraction (XRD) data were collected using an incident x-ray beam of 3×3 μm^2 full width at half maximum (FWHM) spot on an EIGER detector and a wavelength of 0.4104 Å (ID15b) and an incident x-ray beam of 2.3×2.6 μm^2 FWHM spot on a MAR-CCD detector and a wavelength of 0.3738 Å (ID27), both calibrated using a reference CeO_2 sample. The bidimensional images were integrated using DIOPTAS software [33].

Two types of data acquisition were performed: panoramic and multiexposure. Panoramic patterns are recorded while rotating the diamond-anvil cell by $\theta_c = \pm\theta_{max}$ around a vertical axis (see Fig. 1). Multiexposure is the collection of several patterns, each obtained for a smaller rotation range. Angle steps of 0.25° to 2° allow the collection of data all along the rotation of the diamond-anvil cell between $-\theta_{max}$ and $+\theta_{max}$. This enables the determination of crystal orientations at each condition, and consequently of possible OR between phases during phase transformations. In run 1, at some selected pressure steps (6, 13, 14, 17, 9, and 6 GPa), data have been collected all over the sample using a 80×80 μm^2 grid (100 points), allowing a precise microstructural analysis.

C. Postprocessing of XRD data

Data processing was performed with the TIMEless tools software, available from the FABLE project,[1] specifically developed for the processing of DAC experiments, and GrainSpotter for grain indexing [34]. In particular, multigrain analysis, as described in Refs. [35,36], was performed to compute orientations of crystals. This method is based on the automatic detection of diffraction peaks from multiexposure data. Measurements of d spacing, azimuthal angle and rotation angle for each peak is processed and orientations of one to ∼100 single crystals that explain the experimental peaks are suggested. It is quite fast and exhaustive [36].

The different orientations obtained with multigrain analysis are plotted in a pole figure using MTEX toolbox [37] to determine possible OR between phases. In particular, we looked for coincidences within plane orientations ($(110)_{bcc}//(0001)_{hcp}$ and $[111]_{bcc}//[2\bar{1}\bar{1}0]_{hcp}$) to evidence Burgers martensitic OR for the $\alpha \leftrightarrow \epsilon$ transformation as described in [22,24,38]. This mechanism can be described as follows (see Fig. 2): first, a compression in the $(110)_{bcc}$ plane along the $[001]_{bcc}$ direction. The atoms form regular hexagons that will lie in $(0001)_{hcp}$ basal planes. Then, a shuffle of every other $(110)_{bcc}$ plane in the $[\bar{1}10]_{bcc}$ direction takes place to form the hcp structure. As there exists six equivalent $(110)_{bcc}$

[1] https://github.com/FABLE-3DXRD/TIMEleSS

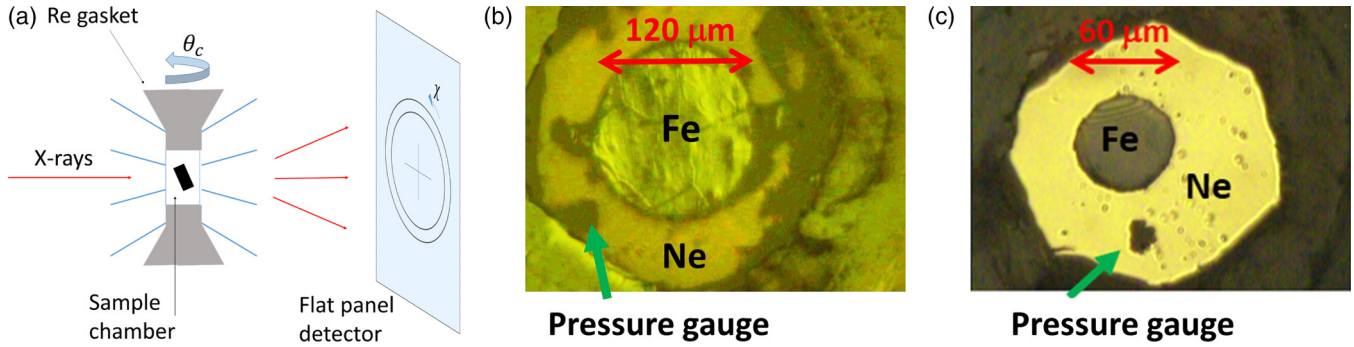

FIG. 1. (a) Experimental angular dispersive x-ray diffraction setup. (b) Picture of run 1 sample loaded in a DAC. (c) Picture of run 3 sample loaded in a DAC.

planes in a bcc structure, six different hcp crystals, called variants, can be obtained from one bcc orientation. Applying this mechanism to numerous grains will induce strong deviatoric stresses that must be relaxed through plastic activity or any other deformation mechanism. To limit atomic displacements one $(1\bar{1}2)_{bcc}//(10\bar{1}0)_{hcp}$ plane (called habit plane) is left unchanged during the phase transformation [8,22,24]. Consequently, a rotation of $\pm 5.3^\circ$ around the $\vec{c}$ axis is experienced by the crystal, and splits each previous hcp crystal into two distinct possible orientations which correspond to two different habit planes. Starting from a single α-Fe orientation, Burgers mechanism provides 12 distinct hcp crystal orientations as presented in Table II; the convention used is the same as in Ref. [24].

During reversion, using the same Burgers OR, one hcp orientation can produce six bcc orientations. However, it has been reported that a single crystal recovers its initial orientation after one $\alpha \rightarrow \epsilon \rightarrow \alpha$ cycle, which has been called a memory effect in the reverse transition mechanism [22]. Here, we call this behavior "Burgers mechanism with memory effect."

D. EBSD

In order to characterize *ex situ* the evolution of grain orientations, electron back scattered diffraction (EBSD) maps were collected on run 1 sample before and after experiment using a MIRA3 TESCAN SEM equipped with an Oxford Symmetry 2 EBSD detector at an acceleration voltage of 20 kV and with an indexation step size of 0.5 µm. Orientations are exported as Euler angles with a Bunge convention [39]. EBSD raw data were processed using the MTEX toolbox [37]. It is used in particular for the computation of grain boundaries and grain mean orientations.

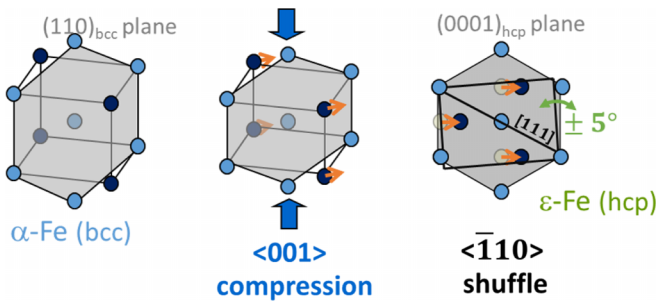

FIG. 2. Schematic representation of Burgers mechanism, with compression and shuffle steps. The unchanged direction [111] belonging to the habit plane is indicated.

III. $\alpha \leftrightarrow \epsilon$ TRANSITION

A. Transformation conditions

Bidimensional panoramic XRD patterns were azimuthally integrated in order to determine phase fractions and measure lattice parameters. Figure 3(a) shows the typical evolution of the integrated patterns during the loading-unloading cycle in the largest grain in Run 1 sample (300 K). α-Fe and ϵ-Fe peaks can be easily identified. Phase relative fractions have been estimated using the intensity ratio between $(002)_{bcc}$ and $(10\bar{1}2)_{hcp}$ peaks. Figure 3(b) presents the evolution of ϵ-Fe fraction during the experiment with a direct comparison with literature [22,24].

The onset of the direct $\alpha \rightarrow \epsilon$ transition is found at 13.1 ± 0.5 GPa and the transition is almost completed at 17.0 ± 0.5 GPa. This range of transformation pressures is consistent with previous XRD studies on a single crystal loaded in neon [22] or a laminated foil loaded in helium [24]. Their respective transition pressure onsets are reported at 13.8 GPa and

TABLE II. Crystallographic definition of the 12 variants obtained during the bcc to hcp phase transition as described by Burgers mechanism. The nomenclature is the same as in [24]. Variants b are obtained by a rotation of 10.6° of variants a around $\vec{c}$ axis.

Plane	Direction	Variant
$(110)_{bcc}//(0001)_{hcp}$	$[1\bar{1}1]_{bcc}//[2\bar{1}\bar{1}0]_{hcp}$	V1.a
	$[\bar{1}11]_{bcc}//[2\bar{1}\bar{1}0]_{hcp}$	V1.b
$(\bar{1}10)_{bcc}//(0001)_{hcp}$	$[11\bar{1}]_{bcc}//[2\bar{1}\bar{1}0]_{hcp}$	V2.a
	$[111]_{bcc}//[2\bar{1}\bar{1}0]_{hcp}$	V2.b
$(101)_{bcc}//(0001)_{hcp}$	$[11\bar{1}]_{bcc}//[2\bar{1}\bar{1}0]_{hcp}$	V3.a
	$[1\bar{1}\bar{1}]_{bcc}//[2\bar{1}\bar{1}0]_{hcp}$	V3.b
$(011)_{bcc}//(0001)_{hcp}$	$[11\bar{1}]_{bcc}//[2\bar{1}\bar{1}0]_{hcp}$	V4.a
	$[1\bar{1}1]_{bcc}//[2\bar{1}\bar{1}0]_{hcp}$	V4.b
$(\bar{1}01)_{bcc}//(0001)_{hcp}$	$[1\bar{1}1]_{bcc}//[2\bar{1}\bar{1}0]_{hcp}$	V5.a
	$[111]_{bcc}//[2\bar{1}\bar{1}0]_{hcp}$	V5.b
$(0\bar{1}1)_{bcc}//(0001)_{hcp}$	$[\bar{1}11]_{bcc}//[2\bar{1}\bar{1}0]_{hcp}$	V6.a
	$[111]_{bcc}//[2\bar{1}\bar{1}0]_{hcp}$	V6.b

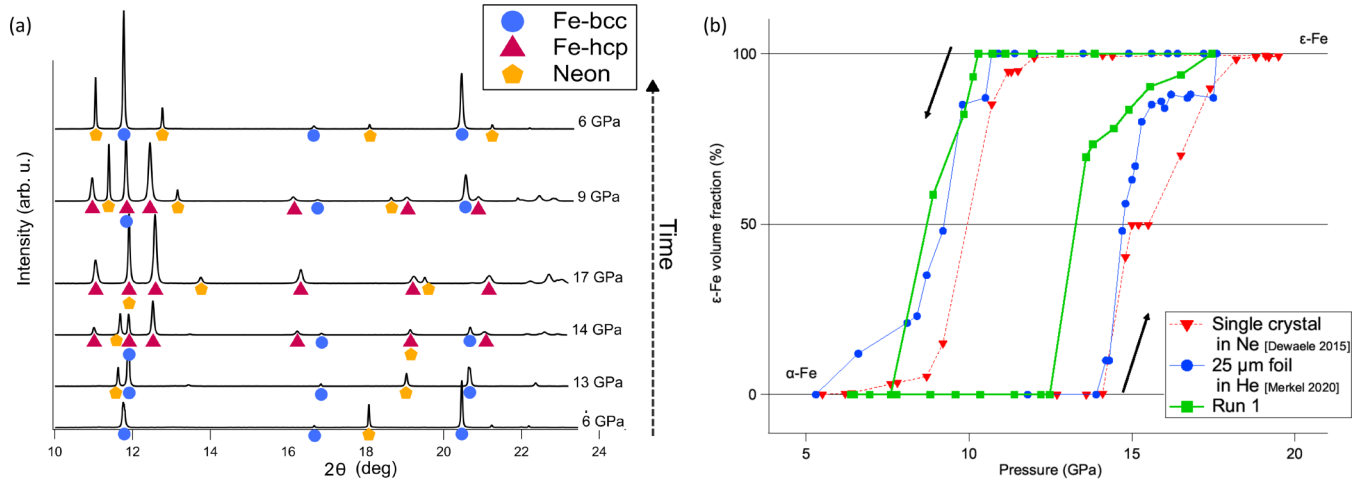

FIG. 3. (a) Evolution of XRD patterns during run 1. 1D patterns are obtained by azimuthal integration of the XRD images inside the largest grain in the sample. (b) Fraction of ϵ-Fe in run 1. It has been estimated using the intensity ratio between $(002)_{bcc}$ and $(10\bar{1}2)_{hcp}$ peaks. Litterature data are also plotted as blue circles for an untreated foil [24], and as red triangles for a single crystal [22].

14.0 GPa. This is slighlty higher than in our experiment but the difference can be due to the different sample preparation (heat treatment in our sample). Note the large pressure difference between 50% and complete $\alpha \rightarrow \epsilon$ transformation ($\sim$3 GPa) for all runs represented in Fig 3.

The reverse $\epsilon \rightarrow \alpha$ transition starts at 10.3 ± 0.5 GPa and finishes at 6.9 ± 0.5 GPa. Both hysteresis and α-ϵ coexistence domain are in agreement with results from the literature [22,24], as well as the fact that a small amount of bcc phase remains at high pressure. The start of the $\alpha \rightarrow \epsilon$ transition is sensitive to starting sample microstructure and pressuring conditions; $\epsilon \rightarrow \alpha$ is less sensitive.

B. Microstructure in α-Fe and ϵ-Fe

EBSD mappings and SEM observations were performed before loading run 1 sample in the DAC. They are displayed in Fig. 4. Grain boundaries are highlighted in order to visualize the four main grains. Nonindexed area (with no color on EBSD maps) are caused either by the presence of small stripes or dust on the surface. EBSD orientation maps show that the sample exhibits preferred orientations as a result of rolling process. We identify four large and undeformed grains, with the [100] direction almost parallel to the normal of the sample, which is also the compression axis in the DAC.

After experiment, the same measurements were performed. Grain boundaries are almost unchanged and overall orientation is preserved all over the surface [22] (Fig. 4). However, continuous orientation gradient (orientation variations up to 5° inside the same grain) within grains evidence a higher level of mosaicity than before the experiment. Plastic strain may account for the surface upveals on Fig. 4(b).

A direct observation of plasticity using image plates obtained by XRD shows an acute broadening of peaks due to the transition [Fig. 5(a)]. In particular, a qualitative analysis can be performed through the evolution of a diffraction spot from α-Fe integrated along the azimuthal angle χ [Fig. 5(b)]. During loading, from 6 to 13 GPa (just before transition), diffraction spots remain intense and circular, typical of a high quality single crystal. As soon as the transformation begins, they widen to $\sim$3° FWHM along the azimuthal and rotation of the cell angles. This width is preserved during unloading. This peak enlargement is consistent with the mosaicity observed on recovered samples and with other measurements performed on single crystals under static or shock compression [16,22].

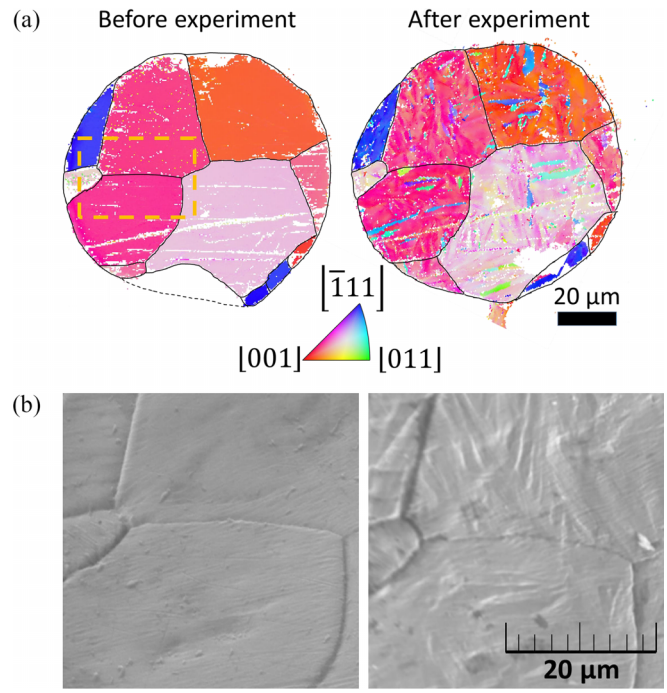

FIG. 4. (a) EBSD maps of run 1 sample before and after experiment. Orientations are color-coded according to the adjacent key z-axis inverse pole figure. Grains boundaries are marked by black lines. White areas correspond to nonindexed data (due to local deformation, dust or small stripes). (b) SEM images of the sample before and after the experiment: zoom in the area indicated by orange box in (a). Roughness with shape of lenticular grains is observed after the experiment.

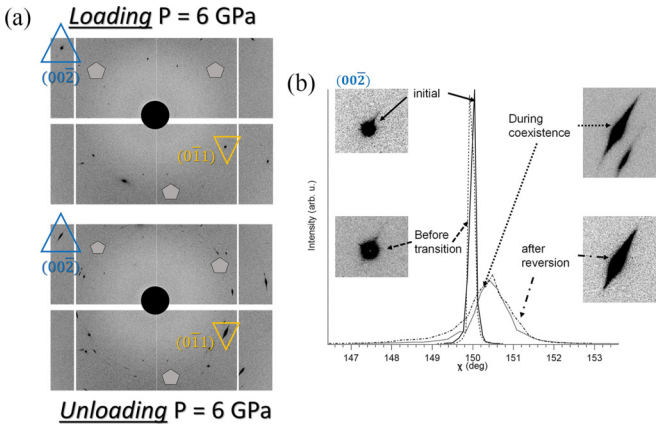

FIG. 5. (a) XRD images of α-Fe before and after $\alpha \rightarrow \epsilon \rightarrow \alpha$ transformation at the same location on run 1 sample and at 6 GPa. (00$\bar{2}$) and (0$\bar{1}$1) peaks of the same crystals are indicated. (b) Profile in χ azimuthal angle of (00$\bar{2}$) peaks before transition (6 and 13 GPa), during coexistence bcc-hcp and back at 6 GPa.

Plasticity is consequently an important deformation mechanism during the transformation.

Almost 5% of the surface area presents orientations that completely differ from the starting one. These grains have a lenticular shape with a length between 4 and 20-μm and a width up to 5-μm. Note that very thin lenticular grains could fall below the resolution of the presented EBSD data. In what follows, two cases are distinguished: orientations reverting to almost the initial orientation are associated with a memory effect; the others to a loss of memory effect.

C. Memory $\alpha \rightarrow \epsilon \rightarrow \alpha$ mechanism

In situ multigrain analysis allows the determination of every orientation in the ϵ phase. Then, crystal OR between parent α-Fe and daughter ϵ-Fe phases during the transition can be calculated. A schematic representation of the evolution of crystal orientations is plotted in Fig. 6 for one location in the sample.

Starting from a single α-Fe orientation, 5 ϵ-Fe orientations appear as soon as the transition begins (∼14 GPa). As the pressure increases, another orientation is formed (variant V4.b). Every ϵ-Fe orientation can be linked to the starting one using Burgers mechanism as described above (see Methods section); they are thus variants of the martensitic transformation. During unloading, a single α-Fe orientation, which is the same as at the beginning of the experiment, is formed. Again, the reverse $\epsilon \rightarrow \alpha$ transformation presents a large transition domain, with some orientations experiencing their phase transition at 9 GPa (V4.a, V4.b, and V5.b) and the other at smaller pressures (V1.b, V3.a, and V6.b).

Figure 7(a) shows a small volume ($7 \times (3 \times 3 \times 10\ \mu m^3)$) of ϵ-Fe sample with different colours for each variant. An example for the determination of variants is displayed on Fig. 7(b). We represent here two unrolled images used for the determination of variant associated with a simulated diffraction pattern. The position of the Bragg spots expected for Burgers path were simulated using the tools available in the FABLE project and are compared with measured spots. In the volume displayed in Fig. 7(a), almost all possible 12 variants

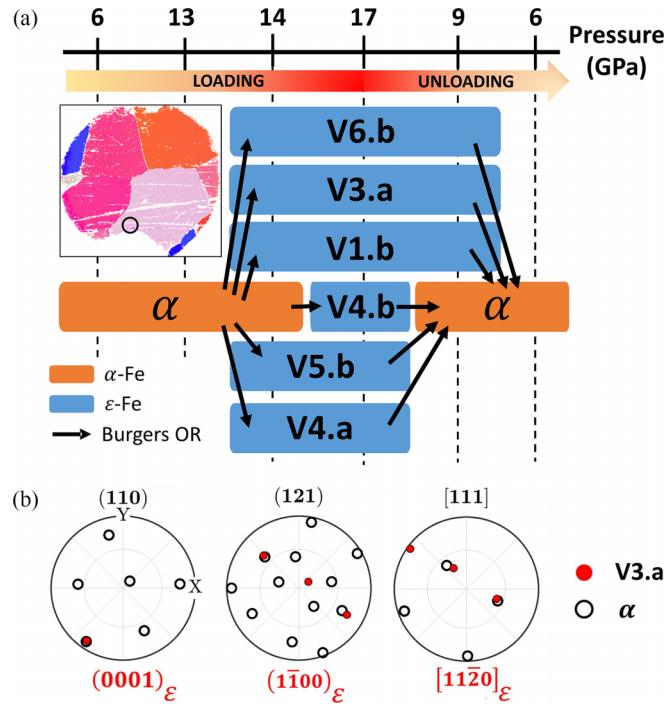

FIG. 6. (a) Schematic representation of the evolution of grain orientations at one position showing a perfect Burgers mechanism with memory effect in the reversion. This evolution is typical of 95% of the sample. The pressure scale shows the six steps where the sample was fully mapped for multigrain analysis. Rectangular bars represent the pressure domains where α-Fe and each variant of of ϵ-Fe have been observed, constrained by these six pressure steps. Nomenclature for ϵ-Fe variants is based on Table II. (Inset) Location of the diffraction spot for the current analysis. (b) Pole figures of one ϵ-Fe orientation (V3.a) used to determine Burgers relationship with the initial α orientation. In pole figures, X is the compression axis.

are observed, sometimes with adjacent locations that suggest a grain size reaching 10 μm. It is interesting to note that 10 μm is also the smallest dimension of the samples. With larger 800-μm samples, ϵ-Fe grains with dimensions of several hundreds of micrometers were observed [8]: the microstructure scales with sample dimension. The lack of variant selection and a random distribution of variants is consistent with previous study performed on single crystals with compression axis in [100] direction [8,22]. A clear variant selection is reported under uniaxial dynamic loading [16,17]: variants with *c* axis perpendicular to loading along $[100]_{bcc}$ direction are favoured. With hydrostatic conditions, all directions are equally compressed. One thus expects that hydrostatic conditions lead to no variant selection. However, a recent study by Ishimatsu *et al.* [25] reports strong variant selection in single crystal compressed in helium: only the three variants with the habit plane perpendicular to the [111] sample surface are observed, which is interpreted by the existence of a small nonhydrostatic compression effect to induce variant selection. Here, we do not see such an effect. The main differences with our experiments are the sample surface normal direction ([111] in Ref. [25], close to [100] here) and the sample thickness and thickness over diameter ratio (≃3 in Ref. [25], ≃10 here). Ishimatsu *et al.*

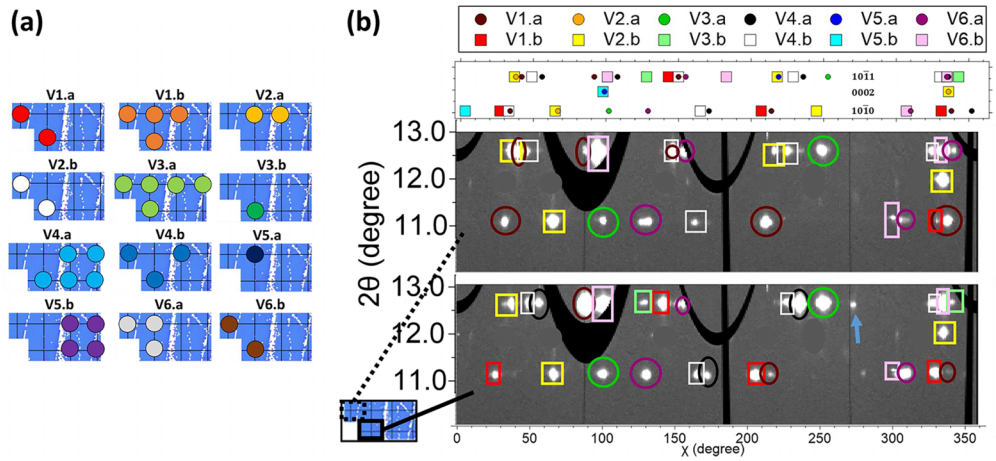

FIG. 7. (a) Distribution of the locations where each variant of ϵ-Fe listed in Table II can be detected at 17 GPa. Seven adjacent points in the same grain of α-Fe mesh are represented. A dot signals the presence of the variant in the scanned volume (spot size 3×3 μm^2 and thickness 10 μm). The analysis shows that there is no apparent variant selection even at a small scale. (b) Comparison between XRD data and prediction of Burgers model for two locations from (a) (see inset). Top panel displays a simulated diffraction pattern based on Burgers model and starting α-Fe orientation. Middle and bottom panels display unrolled XRD images vs azimuth χ and diffraction 2θ angles. The color of the circles/squares corresponds to the assignment of the top panel. Blue arrow indicates diffraction peak that could not be identified using simple Burger path. XRD peaks from neon pressure medium have been masked with grey discs.

suggest that small nonhydrostatic compression effect induce the variant selection, which implies that the transition is more sensitive to uniaxial stress along [111] direction than [100] direction. We also note that a combination of the three variants observed by Ishimatsu *et al.* allow the crystal to complete the $\alpha\rightarrow\epsilon$ phase transformation without any global deformation (as in the case of twinning), which should reduce the transition energy. Our data are not sufficient to distinguish between shape change effect and crystal orientation effect.

The clear existence of an OR between the two phases associated with large plasticity confirm that the $\alpha\rightarrow\epsilon$ transition in iron is martensitic. Here we further constrain the microstructure induced by the transition: ϵ-Fe lenticular crystals with typical size up to 10-μm appear with no variant selection in α-Fe single crystals. Shape mismatches are released via dislocations activity. At reversion, the system mostly returns back to its starting orientation. This variant selection probably allows the system to minimize energy through the transformation because it releases shape mismatches and stresses. As a matter of fact, when the transition is monitored visually, large surface upveals typical of martensitic mechanisms appear/disappear on $\alpha\rightarrow\epsilon/\epsilon\rightarrow\alpha$ transformation [25]. Other defects (impurities, pinned dislocations) could help trigger $\epsilon\rightarrow\alpha$ transition on the same path as the direct one.

D. $\alpha\rightarrow\epsilon\rightarrow\alpha$ without memory mechanism

The orientation of lenticular α-Fe grains differ from the starting α-Fe grain (see Fig. 4). We performed an OR analysis at eight different locations all over the sample, all on lenticular grains, that yield similar results.

A schematic representation of an *in situ* analysis performed at one of these locations is presented on Fig. 8. Starting from a single α-Fe orientation, five orientations of ϵ-Fe appear as the pressure increases. Four orientations (Burgers V1.a, V2.b, V3.a, and V4.b) are formed as soon as the transition begins, and the last one (Burgers V5.b) is formed at higher pressure. During the reverse transition, a second bcc orientation (named α' in Fig. 8), is formed. This orientation agrees with EBSD measurements on the recovered sample. α' can be related to one ϵ-Fe orientation (V4.b) using Burgers reversion OR. The lenticular grain can thus be the result of a Burgers mechanism without memory effect as described in section methods. Wang *et al.* [38] use "transformation twinning" expression to characterize this OR. For clarity with respect to twinning systems in the hcp phase discussed below, we decided not to use this term.

It is interesting to note that two twinning systems ($\{10\bar{1}1\}\langle10\bar{1}\bar{2}\rangle$ and $\{10\bar{1}3\}\langle30\bar{3}\bar{2}\rangle$) out of seven reported in the literature [40] yield OR that are observed between two Burgers variants (V4.b and V1.a). Figure 8 presents the orientation of $(110)_{\text{bcc}}$ and $(10\bar{1}1)_{\text{hcp}}$ planes showing both Burgers OR and twinning OR between α-Fe, V1.a and V4.b. In the present case, with a c/a ratio close to 1.61, a rotation of 120.7° (resp. 120.6°) instead of 123° (resp. 116°) according to [40] is used to correlate the two variants with the $\{10\bar{1}1\}\langle10\bar{1}\bar{2}\rangle$ (resp. $\{10\bar{1}3\}\langle30\bar{3}\bar{2}\rangle$) twinning system—the two twinning systems are equivalent within 7° [40]. The $\{10\bar{1}1\}\langle10\bar{1}\bar{2}\rangle$ twinning system is the most reported in the literature [41], is closer to experimental observation and can occur as a result of high stresses induced by the martensitic transformation [4]. Based on twinning observation, we can still propose a second formation path for the lenticular grain: $\alpha \xrightarrow{\text{Burgers}} V1.a \xrightarrow[\{10\bar{1}1\}\langle10\bar{1}\bar{2}\rangle]{\text{Twinning}} V4.b \xrightarrow{\text{Burgers}} \alpha$. Twinning in ϵ-Fe could explain the diffraction peak from Fig. 7(b) highlighted with blue arrows. We were not able to determine a crystal orientation from this peak. Checking all possibilities from twinning seems unrealistic as it will cover a large part of the reciprocal space.

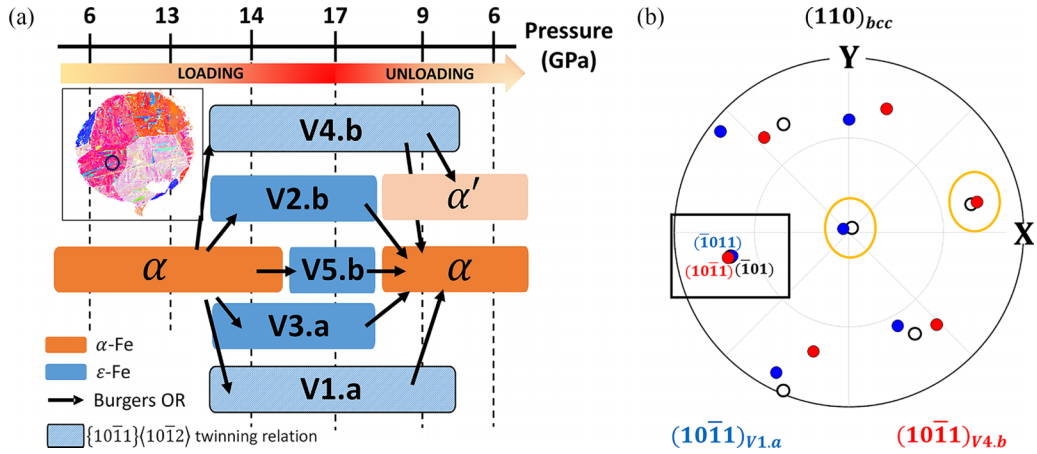

FIG. 8. (a) Schematic representation of the evolution of grain orientations in one region where a lenticular grain with different orientation was detected after unloading (see inset). The pressure scale shows the six steps where the sample was fully mapped for multigrain analysis. Rectangular bars represent the pressure domains where α-Fe and each variant of of ϵ-Fe have been observed, constrained by these six pressure steps. New α' orientation is related to V4.b by Burgers OR. V1.a and V4.b are related by $\{10\bar{1}1\}\langle 10\bar{1}2\rangle$ twinning OR. (b) Pole figure showing pole coincidence between V1.a (blue dots), V4.b (red dots), and α (dark circles). The twinning relation leaves one $(10\bar{1}1)_{hcp}$ plane unchanged. In the square box, $(110)_{bcc}//(10\bar{1}1)_{V1.a}//(10\bar{1}1)_{V4.b}$ planes are highlighted. The latter is the twinning plane in $\{10\bar{1}1\}\langle 10\bar{1}2\rangle$ hcp twinning system. Two other $(10\bar{1}1)_{hcp}$ planes in V1.a and V4.b coincide with different $(110)_{bcc}$ planes (orange circles). X is the compression axis.

The lenticular shape of the α'-Fe grain is similar to the shape of ϵ-Fe grains observed *in situ* with X-ray tomography [8], as well as grains recovered from shock-loaded sample after partial transformation to ϵ-Fe [38]. This suggests that one α'-Fe grain corresponds to one ϵ-Fe grain formed by Burgers mechanism. We checked this assumption by measuring the orientation between the intersection of that surface and the sample surface using EBSD. If they correspond to one ϵ-Fe grain, the surface should be close to a $(112)_{bcc}$ plane, which is the habit plane of the transformation [4,22,38,42]. Measurements on EBSD show that the surface is indeed perpendicular, within less than 4 degrees, to a $[112]_{bcc}$ direction (see Ref. [43]), confirming our hypothesis. Boundaries inside lenticular grains could be observed with EBSD, but the resolution is too low to measure their orientation and check whether they can be attributed to $\{10\bar{1}1\}\langle 10\bar{1}\bar{2}\rangle$ hcp twinning or to Burgers without memory as described in Ref. [38]. It can be noted that in the study by Wang *et al.* [38] study, the proportion of $\alpha\rightarrow\epsilon\rightarrow\alpha$' is much higher (~55%) than in the present study (~5%).

IV. $\alpha\rightarrow\gamma\rightarrow\epsilon$ TRANSITION

A. $\alpha\rightarrow\gamma$ transformation

The $\alpha\rightarrow\gamma$ transition of a single crystal of α-Fe has been induced in seven experiments (run 2 → run 8), around 6-10 GPa by temperature increase on seven-crystal and single-crystal samples. The temperature range of the transformation was 773–796 K, with a coexistence range of ~20 K. These conditions agree with the phase diagram in Ref. [9].

The starting single crystal transformed into numerous grains of γ-Fe with various sizes down to submicrometer; due to a lack of beamtime, γ-Fe samples were not systematically mapped with XRD. The orientation of only the largest one(s) (which could reach 15 microns) was measured. The rocking curves of γ-Fe crystals formed by the transition were relatively narrow, indicating a good crystal quality. Image plates before and after the temperature-induced transition are presented in Fig. 10.

We determined 12 α-γ OR; among them four pairs of γ-Fe crystals were identified, close to each other within XRD spot size (3 μm), with a clear relation: a rotation by 60° around a (111) axis. This corresponds to a stacking fault along the dense plane of fcc crystals: BCABCACBACB... and can also be viewed as a $\{111\}\langle 11\bar{2}\rangle$ twin [40,44]. The XRD signal from one of these pairs is provided in Fig. 10.

Three main martensitic mechanisms for bcc-fcc transformations were found in the literature: Bain, Nishiyama-Wassermann, and Kurdjumov-Sachs, the last two being reported for the majority of iron alloys [4,45,46]. Their OR are shown in Fig. 9: in particular, one $(100)_{bcc}//(100)_{fcc}$ for Bain mechanism and one $(110)_{bcc}//(111)_{fcc}$ for Nishiyama-Wassermann and Kurdjumov-Sachs mechanisms. Only 3 (out of 12) α-γ OR were close (within 5°, the estimated accuracy of the current orientation measurements) to one of them. Figure 10(b) shows one example where none of these OR was found within at least 12°. This lack of coincidence between martensitic OR and measured OR, together with the observation of stacking faults (or $\{111\}\langle 11\bar{2}\rangle$ twins) which are common recrystallization features for fcc crystals [44] and the good crystal quality, suggest a reconstructive (rather than martensitic) transition mechanism for the α-Fe→γ-Fe transformation.

This reconstructive scenario is in line with a recent *in situ* measurement of the microstructure induced by this transition under similar conditions in a large volume device [8]. In this study, a few γ-Fe crystals formed from a α-Fe single crystals, with no martensitic OR. We note that a monitoring of the transformation made at ambient pressure evidenced a disappearance of α-Fe crystallographic order before the crystallization of γ-Fe [1], also not compatible with a martensitic mechanism. Temperature-induced softening of phonon modes

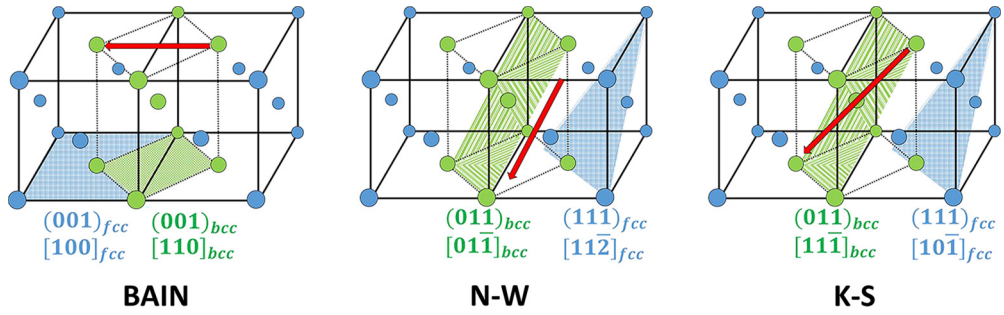

FIG. 9. Bain, Nishiyama-Wasserman (NW), and Kurdjumov-Sachs (KS) OR between the bcc phase (green dots) and the fcc phase (blue dots) [4]. The red arrows indicate the invariant directions during the phase transformation.

in α-Fe are reported at ambient pressure [6], we do not know if this is also the case under high pressure, where structural and magnetic transitions take place concomitantly [47].

To sum up, experimental evidences collected in various devices point to a reconstructive scenario for the $\alpha \rightarrow \gamma$ transformation under ambient and high pressure, up to the α-γ-ϵ triple point.

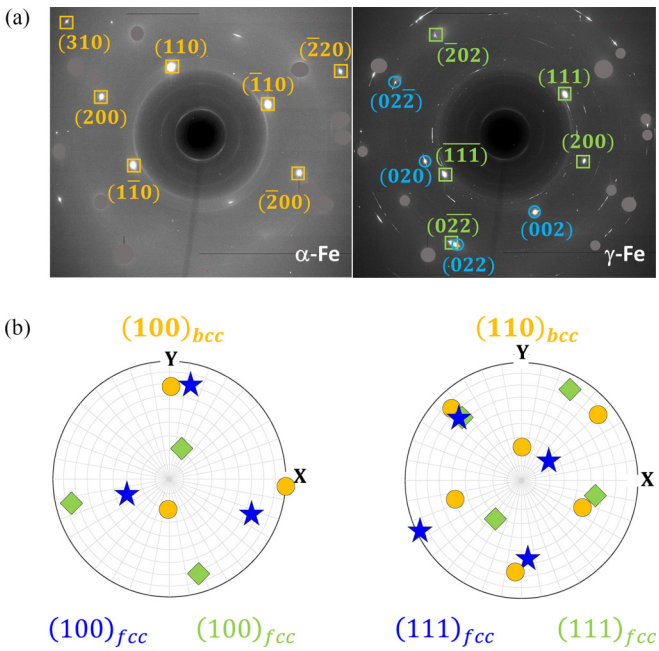

FIG. 10. $\alpha \rightarrow \gamma$ transformation with formation of twinned crystals in run 8. (a) XRD signal collected at 212 °C, 6.4 GPa (left) and 532 °C, 7.0 GPa (right). α-Fe single crystal XRD peaks are marked by orange squares; two γ-Fe single crystals XRD peaks are marked by blue circles and green squares. Note that two (022) peaks of these crystals coincide as expected for $\{111\}\langle 11\bar{2}\rangle$ twins (stacking faults). Numerous small γ-Fe crystals give rise to continuous XRD ring sections. Red circles hide intense XRD peaks from the diamond anvils. The diffuse rings arise from the kapton windows of the vacuum enclosure. (b) Pole figures with the three grains identified on image plates. α-Fe is represented as yellow dots, γ-Fe are represented as green squares and blue stars, with respect to the identification on image plates. X is the compression axis.

B. $\gamma \rightarrow \epsilon$ transformation

The $\gamma \rightarrow \epsilon$ transition was induced by pressure increase around 500 °C–530 °C. It is very sluggish, with 3 GPa to 5 GPa γ-Fe/ϵ-Fe coexistence domains. Even beyond this domain, small amounts of γ-Fe could be detected far in the stability range of ϵ-Fe. The large metastability of γ-Fe has been reported elsewhere [9,47,48].

XRD data for runs 3 and 8 are presented in Fig. 11. In Fig. 11(a), diffuse scattering between x-ray diffraction spots of the parent and child phase in the coexistence domain suggest a transition mechanism involving stacking faults to produce ABAB (hcp) from ABCABC (fcc) stacking with accompanying disorder [49]. Less diffuse scattering is observed in Fig. 11(b), which could be due to the different detector. In both cases, OR corresponding (within experimental uncertainties) to Shoji-Nishiyama relationships were observed (where $(111)_{\mathrm{fcc}}//(0001)_{\mathrm{hcp}}$, $[1\bar{1}0]_{\mathrm{fcc}}//[11\bar{2}0]_{\mathrm{hcp}}$ [4]). Pressure-induced $\gamma \rightarrow \epsilon$ phase transition mechanism is thus likely martensitic; however, no dramatic increase of XRD spots rocking curves is measured suggesting no extensive plastic straining by dislocations emission. Transformation strain might be released by the stacking faults evidenced during the transformation.

V. DISCUSSION

The $\alpha \rightarrow \epsilon$ transition has been studied with various experimental procedures and general features can be inferred from the comparison between current observations and literature reports [8,16–19,22,24,25,38]. In all cases, the transition is reported as martensitic with large parts of the sample following Burgers OR. ϵ-Fe microstructure is constructed of lenticular grains, with size scaling with the starting sample ([8,22,38], this study). Anisotropy in the experiment (uniaxial stress [16,17,25,38], laminated sample [24]) induces a variant selection, which means that all variants predicted by Burgers mechanism are not present in ϵ-Fe [for instance, only two variants are observed after shock loading [16] on a sample with orientation (001)]. Here, all variants are observed under hydrostatic pressurizing conditions. In some experiments, orientations not expected by Burgers path are reported [8,17]: they are interpreted by twinning in ϵ-Fe, induced by the high transformation or pressurizing stresses. The effect of strain rate on twinning remains to be elucidated. In all cases, a high plastic strain via dislocations generation is reported in ϵ-Fe. The reverse $\epsilon \rightarrow \alpha$ transition exhibits a nearly complete

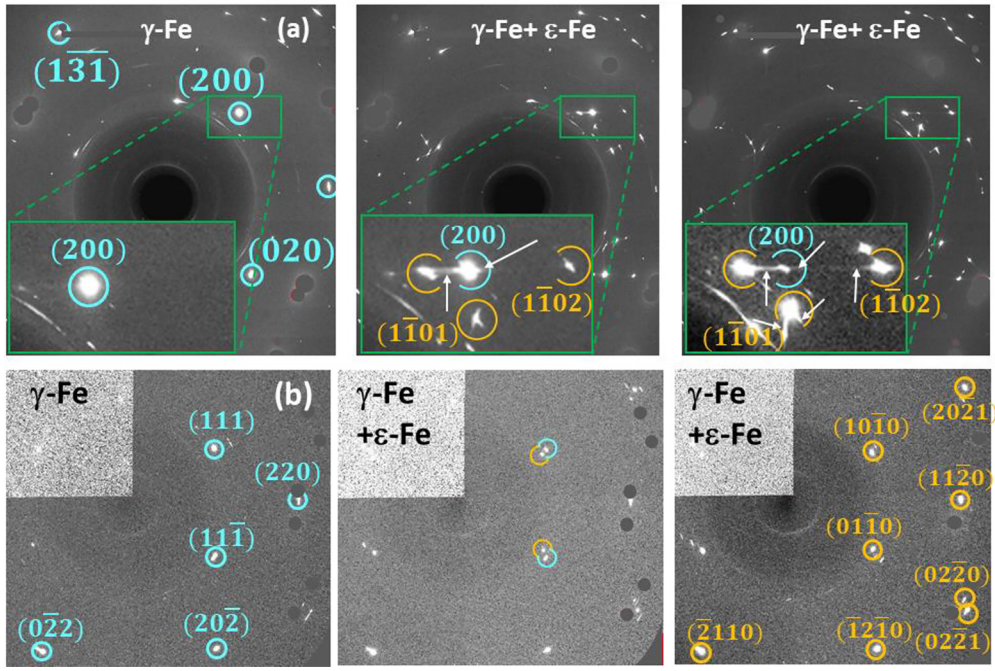

FIG. 11. $\gamma \rightarrow \epsilon$ transformation in run 8 (a) and run 3 (b). (a) panoramic XRD signal collected at 503 °C and 10 GPa (left), 503 °C and 10.5 GPa (middle) and 503 °C and 14.5 GPa (right). (b) panoramic XRD signal collected at 529 °C and 9.5 GPa (left), 529 °C and 10.5 GPa (middle), and 503 °C and 14 GPa (right). XRD peaks of γ-Fe single crystal are marked by blue circles; XRD peaks of ϵ-Fe single crystal(s) are marked in orange (a few crystals in (a), one in (b)). In the two cases, Shoji-Nishiyama OR are observed when single crystals orientation could be determined (in (b): $[220]_{fcc}//[11\bar{2}0]_{hcp}$). In the zoomed regions in (a), diffuse scattering, see white arrows, evidences stacking fault disorder.

memory effect, with a recovery of the starting α-Fe orientation, when performed under static hydrostatic conditions; this suggests that lenticular grains return to starting α-Fe in one step. New orientations within one grain compatible with reverse Burgers path are observed under nonhydrostatic dynamic compression [38], as well as static compression, but in lower amount (Ref. [25], this study).

The $\alpha \rightarrow \gamma$ transition proceeds through a reconstructive mechanism when the temperature is increased smoothly (as here). This mechanism differs from the one observed during the reverse transition induced by rapid quenching under ambient pressure [4]. Time scale is an obvious parameter; however, the difference between the direct and reverse transition, that take place at different temperatures due to the transition hysteresis, also suggests an influence of temperature on the involved mechanism. Increasing temperature favors diffusive process and reconstructive mechanism. Numerous stacking faults in γ-Fe are observed here. It has been suggested that shape constraints on the sample in large volume press device may have favored the reconstructive mechanism (over martensitic) [8]; here, the sample stands in a fluid environment which allows its macroscopic deformation and the transition still proceeds reconstructively. We see no effect of pressure between ambient and 7 GPa on the transition mechanism [8].

The $\gamma \rightarrow \epsilon$ transition is found to be martensitic, with clear Shoji-Nishiyama OR. However, this transformation path produces almost no plasticity compared to the direct $\alpha \rightarrow \epsilon$ transition. As a result, ϵ-Fe single crystals produced by $\alpha \rightarrow \gamma \rightarrow \epsilon$ path are of much higher quality than crystals produced by the direct $\alpha \rightarrow \epsilon$ path.

VI. CONCLUSION

$\alpha \leftrightarrow \epsilon$, $\alpha \rightarrow \gamma$ and $\gamma \rightarrow \epsilon$ transitions have been induced and monitored with X-ray diffraction under hydrostatic compression, at 300 K/7–17 GPa for $\alpha \leftrightarrow \epsilon$, and close to the triple point (8.7 GPa, 750 K) for $\alpha \rightarrow \gamma$ and $\gamma \rightarrow \epsilon$. This has been complemented with ex situ EBSD analysis. Very different transition mechanisms are observed, despite the closeness of P/T range and identical loading procedures.

$\alpha \rightarrow \epsilon$ exhibits all features of martensitic transformations (OR between parent and daughter phase, lenticular grains with expected habit plane), a high plasticity by dislocations activity and the microstructure produced is martensitic, made of highly strained lenticular grains, with size scaling with sample dimensions. It can thus be considered as archetypal of martensitic (or displacive) solid-solid phase transformations; this is interesting as it can be induced by stress or temperature changes and at different rates. $\epsilon \rightarrow \alpha$ is also martensitic but with a strong orientation selection to recover the starting one, except for a minor part of the sample. Twinning in ϵ-Fe might play a role in the variants observed at reversion. $\alpha \rightarrow \gamma$ is very likely reconstructive and γ-Fe recrystallization produces a large amount of stacking faults along dense (111) planes. $\gamma \rightarrow \epsilon$ transition is martensitic as shown by OR and presents little apparent plasticity. Depending on P/T conditions and on the nature of the parent phase, large transformation strains

induced by these martensitic transitions need to be accommodated through plastic activity ($\alpha \rightarrow \epsilon$) or stacking faults ($\gamma \rightarrow \epsilon$).

ACKNOWLEDGMENTS

We acknowledge synchrotron ESRF for the provision of beamtime under proposals HC-2783, HC-3402, and HC-4360. We thank Florent Occelli for his help with samples loading and Jeroen Jacobs for his work on ESRF vacuum heater. The authors would like to thank Sébastien Merkel for kick-starting the multigrain diffraction analysis and early access to the TIMEleSS tools, developed in the framework of the bilateral ANR (France) and DFG (Germany) TIMEleSS project (ANR-17-CE31-0025), and Christophe Denoual for interesting discussions and comments. We thank Mohamed Mezouar for discussions and support.

[1] A. M. Balagurov, I. A. Bobrikov, and I. S. Golovin, Anomalous behavior of an $\alpha \rightarrow \gamma$ phase transition in iron: Results of in situ neutron diffraction experiment, JETP Lett. **107**, 558 (2018).

[2] J. Langner and J. Cahoon, Increase in the alpha to gamma transformation temperature of pure iron upon very rapid heating, Metall. Mater. Trans. A **41**, 1276 (2010).

[3] G. Krauss and A. R. Marder, The morphology of martensite in iron alloys, Metall. Trans. **2**, 2343 (1971).

[4] Z. Nishiyama, *Martensitic Transformation* (Elsevier, Amsterdam, The Netherlands, 2012).

[5] R. Zerwekh and C. Wayman, On the nature of the $\alpha \rightarrow \gamma$ transformation in iron: A study of whiskers, Acta Metall. **13**, 99 (1965).

[6] J. Neuhaus, M. Leitner, K. Nicolaus, W. Petry, B. Hennion, and A. Hiess, Role of vibrational entropy in the stabilization of the high-temperature phases of iron, Phys. Rev. B **89**, 184302 (2014).

[7] N. Bruzy, M. Coret, B. Huneau, L. Stainier, C. Denoual, M. Mondon, and G. Kermouche, Real time imaging of strain fields induced by the ferrite-to-austenite transformation in high purity iron, Mater. Today Commun. **24**, 101028 (2020).

[8] E. Boulard, C. Denoual, A. Dewaele, A. King, Y. Le Godec, and N. Guignot, Following the phase transitions of iron in 3D with X-ray tomography and diffraction under extreme conditions, Acta Mater. **192**, 30 (2020).

[9] A. Dewaele, V. Svitlyk, F. Bottin, J. Bouchet, and J. Jacobs, Iron under conditions close to the $\alpha - \gamma - \epsilon$ triple point, Appl. Phys. Lett. **112**, 201906 (2018).

[10] D. Bancroft, E. L. Peterson, and S. Minshall, Polymorphism of iron at high pressure, J. Appl. Phys. **27**, 291 (1956).

[11] P. M. Giles, M. H. Longenbach, and A. R. Marder, High-pressure $\alpha \rightarrow \epsilon$ martensitic transformation in iron, J. Appl. Phys. **42**, 4290 (1971).

[12] L. M. Barker and R. E. Hollenbach, Shock wave study of the $\alpha \rightarrow \epsilon$ phase transition in iron, J. Appl. Phys. **45**, 4872 (1974).

[13] Q. Wei, C. McCammon, and S. A. Gilder, High-pressure phase transition of iron: A combined magnetic remanence and Mössbauer study, Geochem. Geophys. Geosyst. **18**, 4646 (2017).

[14] D. H. Kalantar, J. F. Belak, G. W. Collins, J. D. Colvin, H. M. Davies, J. H. Eggert, T. C. Germann, J. Hawreliak, B. L. Holian, K. Kadau, P. S. Lomdahl, H. E. Lorenzana, M. A. Meyers, K. Rosolankova, M. S. Schneider, J. Sheppard, J. S. Stölken, and J. S. Wark, Direct Observation of the $\alpha - \epsilon$ Transition in Shock-Compressed Iron via Nanosecond X-ray Diffraction, Phys. Rev. Lett. **95**, 075502 (2005).

[15] J. Hawreliak, J. D. Colvin, J. H. Eggert, D. H. Kalantar, H. E. Lorenzana, J. S. Stölken, H. M. Davies, T. C. Germann, B. L. Holian, K. Kadau, P. S. Lomdahl, A. Higginbotham, K. Rosolankova, J. Sheppard, and J. S. Wark, Analysis of the X-ray diffraction signal for the $\alpha - \epsilon$ transition in shock-compressed iron: Simulation and experiment, Phys. Rev. B **74**, 184107 (2006).

[16] J. A. Hawreliak and S. J. Turneaure, Probing the lattice structure of dynamically compressed and released single crystal iron through the alpha to epsilon phase transition, J. Appl. Phys. **129**, 135901 (2021).

[17] J. A. Hawreliak and S. J. Turneaure, Observations of twinning microstructure in iron ramp-compressed through the $\alpha - \epsilon$ phase transition., Phys. Rev. B **106**, 174306 (2022).

[18] S. Merkel, H.-R. Wenk, P. Gillet, H. kwang Mao, and R. J. Hemley, Deformation of polycrystalline iron up to 30 Gpa and 1000 K, Phys. Earth Planet. Inter. **145**, 239 (2004).

[19] L. Miyagi, M. Kunz, J. Knight, J. Nasiatka, M. Voltolini, and H.-R. Wenk, In situ phase transformation and deformation of iron at high pressure and temperature, J. Appl. Phys. **104**, 103510 (2008).

[20] C. S. Yadav, G. Seyfarth, P. Pedrazzini, H. Wilhelm, R. Cerny, and D. Jaccard, Effect of pressure cycling on iron: Signatures of an electronic instability and unconventional superconductivity, Phys. Rev. B **88**, 054110 (2013).

[21] N. Ishimatsu, Y. Sata, H. Maruyama, T. Watanuki, N. Kawamura, M. Mizumaki, T. Irifune, and H. Sumiya, $\alpha - \epsilon$ transition pathway of iron under quasihydrostatic pressure conditions, Phys. Rev. B **90**, 014422 (2014).

[22] A. Dewaele, C. Denoual, S. Anzellini, F. Occelli, M. Mezouar, P. Cordier, S. Merkel, M. Véron, and E. Rausch, Mechanism of the $\alpha - \epsilon$ phase transformation in iron, Phys. Rev. B **91**, 174105 (2015).

[23] K. Ohta, Y. Nishihara, Y. Sato, K. Hirose, T. Yagi, S. I. Kawaguchi, N. Hirao, and Y. Ohishi, An experimental examination of thermal conductivity anisotropy in hcp iron, Front. Earth Sci. **6**, 176 (2018).

[24] S. Merkel, A. Lincot, and S. Petitgirard, Microstructural effects and mechanism of bcc-hcp-bcc transformations in polycrystalline iron, Phys. Rev. B **102**, 104103 (2020).

[25] N. Ishimatsu, D. Miyashita, and S. I. Kawaguchi, Strong variant selection observed in the $\alpha - \epsilon$ martensitic transition of iron under quasihydrostatic compression along $[111]_{\alpha}$, Phys. Rev. B **102**, 054106 (2020).

[26] W. Burgers, On the process of transition of the cubic-body-centered modification into the hexagonal-close-packed modification of zirconium, Physica **1**, 561 (1934).

[27] D. L. Farber, D. Antonangeli, C. M. Aracne, and J. Benterou, Preparation and characterization of single crystal samples for high-pressure experiments, High Press. Res. **26**, 1 (2006).

[28] G. Shen, Y. Wang, A. Dewaele, C. Wu, D. E. Fratanduono, J. Eggert, S. Klotz, K. F. Dziubek, P. Loubeyre, O. V. Fat'yanov, P. D. Asimow, T. Mashimo, and R. M. M. Wentzcovitch, Toward an international practical pressure scale: A proposal for an IPPS-Ruby gauge (IPPS-RUBY2020), High Press. Res. **40**, 299 (2020).

[29] F. Datchi, R. LeToullec, and P. Loubeyre, Improved calibration of the SrB_4O_7:Sm^{2+} optical pressure gauge: Advantages at very high pressures and high temperatures, J. Appl. Phys. **81**, 3333 (1997).

[30] R. G. Burkovsky, I. Bronwald, D. Andronikova, B. Wehinger, M. Krisch, J. Jacobs, D. Gambetti, K. Roleder, A. Majchrowski, A. V. Filimonov, A. I. Rudskoy, S. B. Vakhrushev, and A. K. Tagantsev, Critical scattering and incommensurate phase transition in antiferroelectric $PbZrO_3$ under pressure, Sci. Rep. **7**, 41512 (2017).

[31] W. L. Vos, J. A. Schouten, D. A. Young, and M. Ross, The melting curve of neon at high pressure, J. Chem. Phys. **94**, 3835 (1991).

[32] S. Klotz, J.-C. Chervin, P. Munsch, and G. Le Marchand, Hydrostatic limits of 11 pressure transmitting media, J. Phys. D **42**, 075413 (2009).

[33] C. Prescher and V. B. Prakapenka, DIOPTAS: A program for reduction of two-dimensional x-ray diffraction data and data exploration, High Press. Res. **35**, 223 (2015).

[34] S. Schmidt, *GrainSpotter*: A fast and robust polycrystalline indexing algorithm, J. Appl. Cryst. **47**, 276 (2014).

[35] A. D. Rosa, N. Hilairet, S. Ghosh, G. Garbarino, J. Jacobs, J.-P. Perrillat, G. Vaughan, and S. Merkel, In situ monitoring of phase transformation microstructures at Earth's mantle pressure and temperature using multi-grain XRD, J. Appl. Cryst. **48**, 1346 (2015).

[36] C. Langrand, N. Hilairet, C. Nisr, M. Roskosz, G. Ribarik, G. B. M. Vaughan, and S. Merkel, Reliability of multigrain indexing for orthorhombic polycrystals above 1 Mbar: application to $MgSiO_3$ post-perovskite, J. Appl. Cryst. **50**, 120 (2017).

[37] F. Bachmann, R. Hielscher, and H. Schaeben, Grain detection from 2D and 3D EBSD data-specification of the MTEX algorithm, Ultramicroscopy **111**, 1720 (2011).

[38] S. J. Wang, M. L. Sui, Y. T. Chen, Q. H. Lu, E. Ma, X. Y. Pei, Q. Z. Li, and H. B. Hu, Microstructural fingerprints of phase transitions in shock-loaded iron, Sci. Rep. **3**, 1086 (2013).

[39] H.-J. Bunge, Texture analysis in materials science, in *Texture Analysis in Materials Science*, edited by H.-J. Bunge (Butterworth-Heinemann, Oxford, UK, 1982), pp. 3–41.

[40] Y. Li, L. Wan, and K. Chen, A look-up table based approach to characterize crystal twinning for synchrotron X-ray Laue microdiffraction scans, J. Appl. Cryst. **48**, 747 (2015).

[41] M. H. Yoo, Slip, twinning, and fracture in hexagonal close-packed metals, Metall. Trans. A **12**, 409 (1981).

[42] G. Seward, S. Celotto, D. Prior, J. Wheeler, and R. Pond, In situ SEM-EBSD observations of the hcp to bcc phase transformation in commercially pure titanium, Acta Mater. **52**, 821 (2004).

[43] See Supplemental Material at http://link.aps.org/supplemental/10.1103/PhysRevB.107.104105 for an example of measurement of habit plane using EBSD maps.

[44] A. Kelly and K. M. Knowles, *Crystallography and Crystal Defects*, 2nd ed. (John Wiley and Sons, Hoboken, NJ, 2012).

[45] G. Nolze, Characterization of the fcc/bcc orientation relationship by EBSD using pole figures and variants, Int. J. Mater. Res. **95**, 744 (2022).

[46] H. J. Bunge, W. Weiss, H. Klein, L. Wcislak, U. Garbe, and J. R. Schneider, Orientation relationship of Widmannstätten plates in an iron meteorite measured with high-energy synchrotron radiation, J. Appl. Cryst. **36**, 137 (2003).

[47] A. Dewaele and L. Nataf, Magnetic phase diagram of iron at high pressure and temperature, Phys. Rev. B **106**, 014104 (2022).

[48] T. Komabayashi, Y. Fei, Y. Meng, and V. Prakapenka, In-situ X-ray diffraction measurements of the γ-ϵ transition boundary of iron in an internally-heated diamond anvil cell, Earth Planet. Sci. Lett. **282**, 252 (2009).

[49] A. D. Rosa, A. Dewaele, G. Garbarino, V. Svitlyk, G. Morard, F. De Angelis, M. Krstulović, R. Briggs, T. Irifune, O. Mathon, and M. A. Bouhifd, Martensitic fcc-hcp transformation pathway in solid Krypton and Xenon and its effect on their equations of state, Phys. Rev. B **105**, 144103 (2022).